

# Diagnosing $SO(5)$ Symmetry and First-Order Transition in the $J - Q_3$ Model via Entanglement Entropy

Zehui Deng,<sup>1,\*</sup> Lu Liu,<sup>2,\*</sup> Wenan Guo,<sup>3,4,1,†</sup> and Hai-Qing Lin<sup>5,‡</sup>

<sup>1</sup>Beijing Computational Science Research Center, Beijing 100193, China

<sup>2</sup>School of Physics, Beijing Institute of Technology, Beijing 100081, China

<sup>3</sup>Department of Physics, Beijing Normal University, Beijing 100875, China

<sup>4</sup>Key Laboratory of Multiscale Spin Physics (Ministry of Education),  
Beijing Normal University, Beijing 100875, China

<sup>5</sup>Institute for Advanced Study in Physics and School of Physics, Zhejiang University, Hangzhou 310058, China

(Dated: January 24, 2024)

We study the scaling behavior of the Rényi entanglement entropy with smooth boundaries at the phase transition point of the two-dimensional  $J - Q_3$  model. Using the recently developed scaling formula [Deng *et al.*, Phys. Rev. B **108**, 125144 (2023)], we find a subleading logarithmic term with a coefficient showing that the number of Goldstone modes is four, indicating the existence of the spontaneous symmetry breaking from an emergent  $SO(5)$  to  $O(4)$  in the thermodynamic limit, but restored in a finite size. This result shows that the believed deconfined quantum critical point of the  $J - Q_3$  model is a weak first-order transition point. Our work provides a new way to distinguish a state with spontaneously broken continuous symmetry from a critical state. The method is particularly useful in identifying weak first-order phase transitions, which are hard to determine using conventional methods.

*Introduction.*—Deconfined quantum criticality (DQC), which describes continuous phase transition between two unrelated ordered states, is beyond the paradigm of Landau-Ginzburg-Wilson[1, 2]. Sandvik invents the  $J - Q_2$  model[3], which realizes the valence-bond solid (VBS)-Néel transition in two-dimensional (2D) quantum spin systems. The model has no sign problem and, therefore, is amenable to quantum Monte Carlo (QMC) simulations to study DQC. The  $J - Q_3$  model [4] is a variant of the  $J - Q_2$  model showing a similar VBS-Néel transition but with the VBS order enhanced in the VBS phase. Lots of QMC studies of these and other variants of the  $J - Q$  model, as well as three-dimensional classical loop models and fermionic models, have characterized the signatures of the DQC[5–12], and shown that the observed quantum phase transition appears to be continuous.

The Néel-VBS DQC can also be described by a nonlinear sigma model containing a Wess-Zumino-Witten term for the five-component superspin[13]. The leading anisotropy plays the role of the mass term in the field theory, which drives the transition between the Néel and VBS phases. Nahum *et al.* [14] conjecture that all the higher anisotropies are irrelevant in the Renormalization Group sense, and there is an emergent  $SO(5)$  symmetry at the deconfined quantum critical point (DQCP). The conjecture was verified numerically at the DQCP of the loop model[14]. The  $SO(5)$  symmetry has also been shown explicitly at the VBS-Néel transition point of the  $J - Q_6$  model [15]. Unfortunately, the transition is shown to be strongly first-order in sharp contrast to the  $J - Q_2$  and  $J - Q_3$  models.

The conformal bootstrap calculation based on  $SO(5)$  symmetry sets bounds on the correlation-length exponent and the anomalous dimension of a critical point[16].

The exponents of the “continuous” VBS-Néel transitions [3, 9, 10, 17] do not satisfy the bounds, alternative scenarios are suggested: The transition is described by a nonunitary conformal field theory (CFT) with complex fixed points [18, 19]; a multicriticality is involved[20, 21]; or it is precursors to a weak first-order transition[22–24].

Entanglement entropy (EE) is a valuable tool to resolve the puzzle. At the criticality of a (2+1)D system, besides the area law, the scaling of EE has a logarithmic term with a *negative* coefficient when the boundary has sharp corners but no logarithmic term if the boundary is smooth[25]. The scaling behavior of the Rényi EE of the  $J - Q_3$  model at the transition point has been studied recently [26]: a positive corner logarithmic term is found, in sharp contradiction with the prediction of unitary CFT. However, a very recent paper shows that the positive logarithmic term due to corners becomes negative when the tilted bipartitioning is applied [27].

It is worth noting that if the (2+1)D system is ordered with continuous symmetry broken, the scaling of EE also has a logarithmic term with a *negative* coefficient when the boundary has sharp corners[28]. In addition, another logarithmic term with a coefficient proportional to the number of Goldstone modes in the scaling form of EE is present even when the boundary is smooth[29]

$$S_n(L) = aL^{d-1} + \frac{N_G}{2} \ln\left(\frac{\rho_s}{c} L^{d-1}\right) + \gamma_{\text{ord}}, \quad (1)$$

where  $L$  is the system size,  $d$  is the spatial dimension,  $N_G$  is the number of Goldstone modes of the ordered phase,  $\rho_s$  is the spin stiffness, and  $c$  is the spinwave velocity.  $\gamma_{\text{ord}}$  is a universal geometry-dependent finite constant, as all the short-distance physics are absorbed into  $\rho_s$  and  $c$ . Unfortunately, this formula only works at very

large system sizes[30, 31] or the order is very strongly enhanced[30], or the continuous symmetry is  $O(2)$ [32].

In a recent work [33], we propose a modified scaling formula for the EE with smooth boundary

$$S_n(L) = aL^{d-1} + \frac{N_G}{2} \ln(I(L)^{1/2} \rho_s(L)^{1/2} L^{d-1}) + \gamma_{\text{ord}}, \quad (2)$$

where  $I(L)$  is the finite size inertia moment density of the quantum rotor describing the energy spectrum of the  $O(n)$  ordered model. Using this formula, The correct  $N_G/2$  is extracted from data of rather small system sizes for the 2D Heisenberg model and the bilayer Heisenberg model. The reason why Eq.(1) works for  $O(2)$  symmetry is also explained by pointing out the leading order correction in  $I(L)$  vanishes[33].

In this letter, we calculate the Rényi EE  $S_2(L)$  with *smooth* boundaries at the transition point of the  $J - Q_3$  model; the results are shown in Fig. 1. Our data shows the presence of a logarithmic term in the scaling form, which has also been reported very recently[34], but not found when tilted bipartitioning is applied[27]. We then use the modified formula Eq. (2) to show that, at the believed DQCP of the  $J - Q_3$  model, the system bears an emergent  $SO(5)$  symmetry, which is broken spontaneously but restored in a finite size. We first calculate  $\rho_s(L)$ , then determine the inertia moment density  $I(L)$  by calculating magnetization as a function of the magnetic field. These are done via standard QMC simulations. Using  $I(L)$  and  $\rho_s(L)$  as inputs, we fit Eq. (2) to the obtained  $S_2(L)$ . We find  $N_G = 4$  at the transition point, showing the finite-size system has the  $SO(5)$  symmetry, described by the vector formed by the  $O(3)$  Néel order and  $O(2)$  VBS order, breaking into an  $O(4)$  symmetry in the thermodynamic limit. Since the formula applies only to the ordered phase, this also proves that the transition is first order, similar to what happens in the checker-board  $J - Q$  model [35].

*Model and method.*— The  $J - Q_3$  model on a 2D square lattice is described by the following Hamiltonian

$$H = -J \sum_{\langle i,j \rangle} C_{ij} - Q \sum_{\langle ijklmn \rangle} C_{ij} C_{kl} C_{mn} - h \sum_i S_i^z, \quad (3)$$

where  $C_{ij} = \frac{1}{4} - \mathbf{S}_i \cdot \mathbf{S}_j$  is the singlet projector at sites  $i$  and  $j$ . The nearest-neighbor  $J$  terms and the three parallel projector product  $Q$  terms are illustrated in Fig. 2.  $h$  is an external magnetic field. Without the external magnetic field, a phase transition separates the Néel ground state for small  $Q/J$  and the VBS state for large  $Q/J$ . The latest estimate of the transition point is  $Q/J = 1.49153(31)$  [36].

The Rényi EE is defined as

$$S_n(A) = \frac{1}{1-n} \ln \text{Tr}[\rho_A^n], \quad (4)$$

where  $\rho_A = \text{Tr}_{\bar{A}} \rho$  is the reduced density matrix of a subsystem  $A$  with  $\bar{A}$  its complement,  $n$  is the Rényi index(

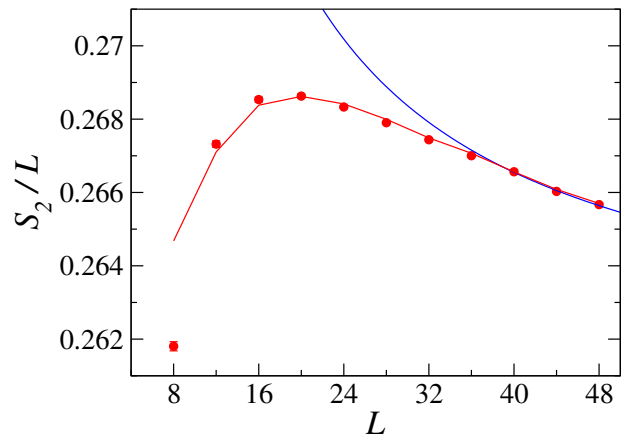


FIG. 1.  $S_2(L)/L$  versus system size  $L$  at  $Q/J = 1.49153$ . The red solid line is the fit of Eq. (2) for  $L \geq L_{\text{min}} = 24$  with  $N_G/2$  found to be 2.01(14), see Tab.III for other parameters. The blue solid line shows the fit without logarithmic corrections for  $L \geq L_{\text{min}} = 40$ , see Tab. I.

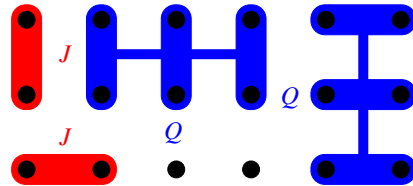


FIG. 2. Illustration of  $J$  terms (light red bars) and  $Q$  terms (three connected blue bars) in the 2D  $J - Q_3$  model.

$n = 2$  in our work).  $\rho = e^{-\beta H}/Z$  is the density operator with  $Z = \text{Tr} e^{-\beta H}$  the partition function.  $\beta \rightarrow \infty$  is the inverse temperature to probe only the properties of the ground states.

In the QMC simulations, we consider an  $L \times L$  square lattice with periodic boundary conditions employed in both lattice directions. In particular, to calculate  $S_2(A)$ , we consider bipartite the toroidal lattice into two equally sized cylindrical strips of size  $N_A = L/2 \times L = N_{\bar{A}}$  containing no corners and study the Rényi EE of one subregion.

We use the nonequilibrium work algorithm developed recently [30] in the version of the projector quantum Monte Carlo (PQMC) method [37, 38] to extract the Rényi EE. In the specific simulations, to guarantee the accuracy of the EE, we compute 2000 to 3000 nonequilibrium work realizations for each system size ranging from  $L = 8$  to  $L = 48$ . Each work realization consists of  $N_A \times 10,000$  nonequilibrium time steps. The projection power  $m = L^3$  in the PQMC simulations.

The spin stiffness  $\rho_s$  is defined as the free energy increasing due to the presence of a twist field. We apply the stochastic series expansion (SSE) QMC simulation with the loop update algorithm at inverse temperature  $\beta = 2L$ [39, 40] to calculate  $\rho_s$  through the fluctuations

of the winding number of spin transporting

$$\rho_s = \frac{n}{4\beta N} \langle L_x^2 W_x^2 + L_y^2 W_y^2 \rangle, \quad (5)$$

where the winding numbers are defined as

$$W_\alpha = (N_\alpha^+ - N_\alpha^-)/L_\alpha. \quad (6)$$

Here,  $N_\alpha^+(N_\alpha^-)$  is the total number of operators transporting spin in the positive (negative)  $\alpha = x, y$  direction.  $N = L_x \times L_y$  is the number of spins. The factor  $n$  is included to account for rotational averaging for the systems with  $O(n)$  symmetry. We have set  $n$  to be the tempted value 5. The choice of  $n$  could change neither the presence of the logarithmic term nor the coefficient of the term, except for  $\gamma_{\text{ord}}$ . Thus, our choice will not bias our conclusion and will show the correct self consistently.

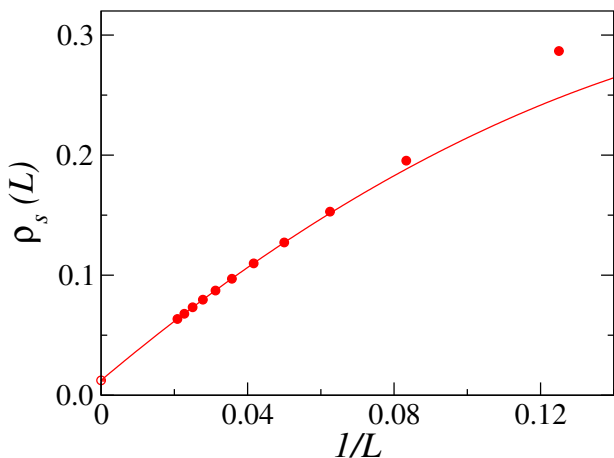


FIG. 3. Spin stiffness  $\rho_s(L)$  versus  $1/L$  at  $Q/J = 1.49153$ . The red solid line is a polynomial fit for data points with  $L \geq 24$ .

In Fig. 3, we show the spin-stiffness  $\rho_s$  for each system size at  $Q/J = 1.49153$ . Polynomial fitting shows  $\rho_s(L)$  converges to a finite value. However, power-law fitting with an exponent  $\sim -0.78$  is also statistically sound. See Ref.[41] for details. This is similar to what is found at the transition point of the  $J - Q_2$  model [24]. For conventional  $(2 + 1)$ D critical behavior,  $\rho_s(L)$  should scale as  $1/L$ . One interpretation of this unusual scaling behavior is that the transition is first order, it can also be accounted for by an unconventional two-length scales scaling scheme[9]. In this work, we do not try to determine or explain the finite-size scaling behavior of  $\rho_s(L)$  and  $I(L)$ . Instead, we use the finite-size value of  $\rho_s(L)$  and  $I(L)$  as inputs of the fitting formula Eq. (2). The results of the fits, in turn, support  $I(L)$  and  $\rho_s(L)$  have finite values at the thermodynamic limit.

To make use of Eq. (2), we need to determine the inertial density  $I(L)$  as well.

Suppose the model is described by  $O(N)$  quantum rotors with  $S$  being the total superspin of the system. The

energy of the tower of excited states is

$$E_L(S) = \frac{S(S + N - 2)}{2L^2 I(L)}, \quad (7)$$

where  $I(L)$  is the inertia moment density and  $L$  is linear size of the system. Here, we have set  $E_L(0) = 0$ .

At the thermodynamic limit,  $I(L)$  converges to the transverse susceptibility  $\chi_\perp$ . The chiral perturbation theory [42] predicts the finite-size behavior of  $I(L)$  up to  $1/L$  [43–45]. However, for the current model, we find the chiral perturbation theory does not work due to the extremely small value of  $\chi_\perp$ , resulting in that the order  $1/L$  is insufficient, see Ref. [41]. We then try to find out the energy levels  $E_L(S)$  and calculate  $I(L)$  from Eq. (7) directly.

This is done by adding a magnetic field and studying the field dependence of the magnetization  $M_z = \langle m_z \rangle$ , with  $m_z = \sum_i S_i^z$ , via the SSE QMC simulation with the directed loop algorithm [46]. When a magnetic field is applied to the system along the direction of one component of the superspin, e.g.,  $S_z$ , the energy levels become

$$E_L(S, m_z) = E_L(S) - h m_z. \quad (8)$$

At a given inverse temperature  $\beta$ , the total magnetization as a function of  $h$  can be calculated using

$$M_z(L, h) = \frac{1}{Z} \sum_{S=0}^{L^2/2} \sum_{m_z=-S}^S m_z g(S, m_z) e^{-\beta E_L(S, m_z)}, \quad (9)$$

with partition function

$$Z = \sum_{S=0}^{L^2/2} \sum_{m_z=-S}^S g(S, m_z) e^{-\beta E_L(S, m_z)}, \quad (10)$$

where  $g(S, m_z)$  is the degeneracy for fixed  $S$  and  $m_z$ . This degeneracy changes with the symmetry [47]. For example,  $g(S, m_z) = 1$  in  $SO(3)$ , however, in  $SO(5)$ ,  $g(0, 0) = 1$ ,  $g(1, 0) = 3$ ,  $g(1, \pm 1) = 1$ ,  $g(2, 0) = 6$ ,  $g(2, \pm 1) = 3$ ,  $g(2, \pm 2) = 1, \dots$  [48]. Fitting Eq. (9) to numerically obtained  $M_z(L, h)$  curve, we can obtain  $E_L(S)$  and  $I(L)$  followed.

Figure 4 shows  $M_z$  as functions of  $h$  for different system sizes  $L$  at  $Q/J = 1.49153$ . In the simulations, the inverse temperature is set to  $\beta = 2L$  to match the lowest rotor levels. We thus find  $E_L(S)$  and  $I(L, S)$ , which depends on  $S$  at finite size, similar to that in the 2D Heisenberg model [45, 46]. However,  $I(L, S)$  for different  $S$  converges to  $I(L)$  for large enough  $L$ , as illustrated in Fig. 5. It is then reasonable to use  $I(L, S = 1)$  as  $I(L)$  when fitting the EE  $S_2(L)$  according to the scaling formula Eq.(2).

As a by-product, we find that  $E_L(S = 2)/E_L(S = 1)$  tends to go to 2.5 and  $E(S = 3)/E(S = 1)$  tends to 4.5 for  $Q/J$  being around 1.489, slightly larger than the estimated transition point  $Q/J = 1.49153(31)$  as  $L$  increases,

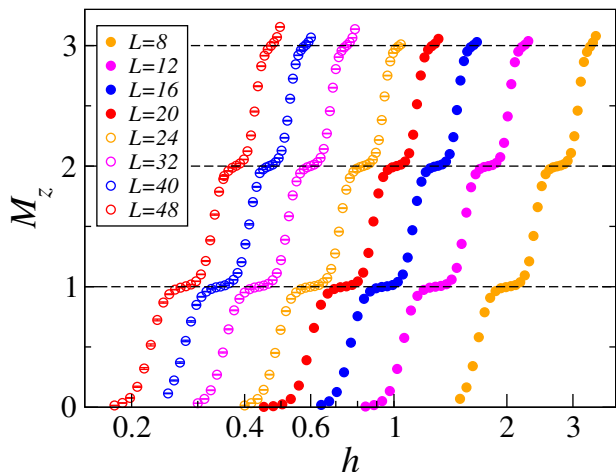


FIG. 4. Total magnetization  $M_z$  versus external magnetic field  $h$  at  $Q/J = 1.49153$  for different system size  $L$ .

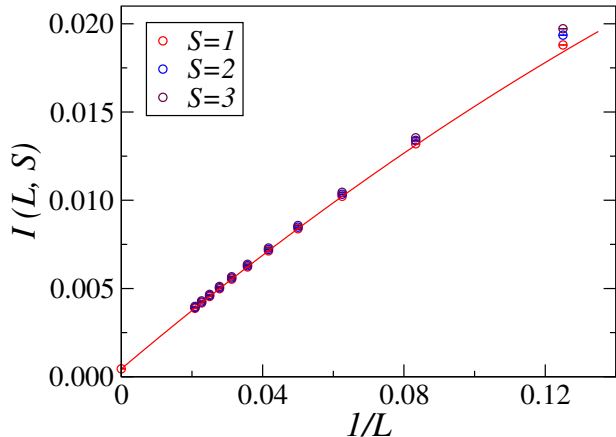


FIG. 5.  $I(L, S)$  of the  $J - Q_3$  model at  $Q/J = 1.49153$ . When  $L$  becomes large,  $I(L, S)$  converges to the same value for different  $S$ , showing the emergence of  $SO(5)$  symmetry. The value  $I(L = \infty, S = 1)$  is found to be  $0.00045(2)$  using a polynomial fit to data points with size  $L \geq 20$  (the red solid line), see [41] for details.

as illustrated in Fig. 6. In the case that the transition point has an emergent  $O(5)$  symmetry, these behaviors indicate the validity of the excitation spectrum Eq. (7) for small  $S$ : as  $L \rightarrow \infty$ ,  $I(L, S)$  converge to  $I(L = \infty)$ , the ratios converge to 2.5 and 4.5, respectively. Meanwhile, it also suggests that  $Q/J = 1.489$  could be the true transition point. We have also done calculations of  $S_2(L)$ ,  $\rho_s(L)$ , and  $I(L, S)$  at  $Q/J = 1.489$ . The results are presented in supplemental materials [41].

*Scaling behavior of  $S_2(L)$  at transition point.*— Suppose the system sits at an ordinary (2+1)D critical point. We expect there to be no logarithm correction to the area law of  $S_2(L)$  since the boundaries separating the subsystem and its complement are smooth. The curve of  $S_2(L)$  in Fig. 1 should be fitted using  $S_2(L)/L = a + c/L$ .

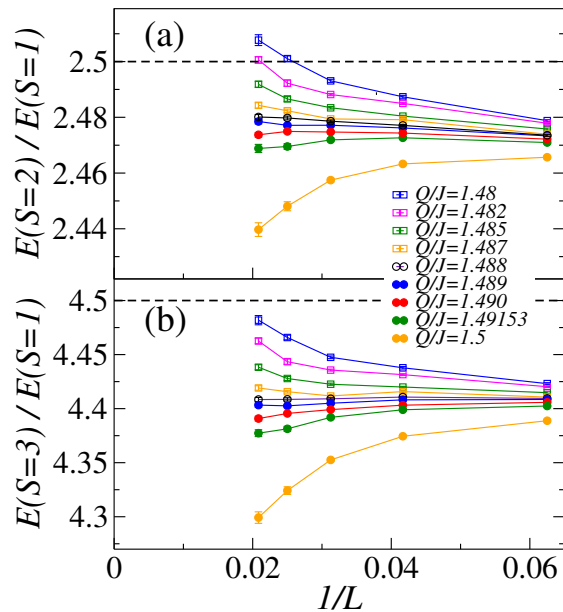


FIG. 6. Energy level ratio versus  $1/L$  for  $Q/J$  near the transition point. (a)  $E(S=2)/E(S=1)$  vs  $1/L$ ; (b)  $E(S=3)/E(S=1)$  vs  $1/L$ . The dash lines indicate ratios of  $SO(5)$  rotor at thermodynamic limit.

Table I shows the results of such fitting. The fits are statistically sound only for the largest three sizes.

TABLE I. Fitting results of  $S_2(L) = aL + c$  to  $S_2(L)$  data at  $Q/J = 1.49153$  with  $L = 8 - 48$ .

$L_{min}$	$a$	$c$	$\chi_r^2/P$ -value
36	0.2616(2)	0.194(6)	3.35/0.035
40	0.2611(3)	0.218(12)	1.32/0.25

On the other hand, we try to fit the data using the following formula with a logarithmic correction term

$$S_2(L)/L = a + b \ln(L)/L + c/L, \quad (11)$$

which is essentially Eq. (1) with  $b = N_G/2$ . Table II shows details of the fitting procedure. The formula can be fitted for all  $L \geq 12$  finite-size data. The presence of a logarithmic correction to the area law is evident. However, the thus found  $b$  is far away from  $N_G/2 = 1$  of the AF ordered phase, nor  $N_G/2 = 2$  of the expected  $SO(5)$  ordered state.

This phenomenon is understandable from the former experience with the 2D AF Heisenberg and the bilayer Heisenberg models. The formula Eq. (1) only works at very large systems, or the order is strongly enhanced [30]. To see the expected logarithmic correction due to Goldstone modes, we have to make use of our improved scaling formula Eq. (2) to the fitting of the finite-size  $S_2(L)$  data. The details of the fitting are shown in Table III. The fits are statistically sound for all  $L \geq 12$  finite-size

TABLE II. Fitting results of Eq. (11) to  $S_2(L)$  at  $Q/J = 1.49153$  with  $L = 8 - 48$ .

$L_{min}$	$a$	$b$	$c$	$\chi_r^2/P$ -value
8	0.2569(1)	0.215(3)	-0.409(5)	2.18/0.03
12	0.2567(2)	0.222(4)	-0.424(10)	1.99/0.05
16	0.2563(3)	0.233(7)	-0.452(17)	1.69/0.12
20	0.2558(4)	0.248(12)	-0.487(30)	1.59/0.16
24	0.2553(6)	0.267(19)	-0.536(46)	1.52/0.19

data. The results of  $N_G/2$  approach 2 within about one error bar for  $L_{min} = 20$ . The fits remain stable upon further excluding small size points by gradually increasing  $L_{min}$ , although error bars on the fit parameters increase rapidly. Thus, we may safely conclude that the system is ordered with  $N_G = 4$ .

We did similar scaling analyses for  $Q/J = 1.489$  and obtained similar results, suggesting the scaling behavior is robust in the neighborhood of the transition point. See Ref. [41] for details.

TABLE III. Fitting results of Eq. (2) to  $S_2(L)$  at  $Q/J = 1.49153$  with  $L = 8 - 48$ . In the fits, finite-size  $\rho_s(L)$  and  $I(L, S = 1)$  are used as inputs. For results obtained using  $I(L, S = 2)$  and  $I(L, S = 3)$ , see [41].

$L_{min}$	$a$	$b$	$\gamma_{ord}$	$\chi_r^2/P$ -value
12	0.2540(2)	1.89(4)	1.10(2)	0.93/0.48
16	0.2543(3)	1.83(6)	1.07(3)	0.82/0.55
20	0.2541(5)	1.88(10)	1.09(5)	0.91/0.47
24	0.2534(7)	2.01(14)	1.16(9)	0.76/0.55
28	0.253(2)	2.1(3)	1.2(2)	0.86/0.46

*Conclusion.*— In this paper, we have studied the scaling behavior of the Rényi EE  $S_2(L)$  with smooth boundaries at the phase transition point of the 2D  $J-Q_3$  model. We have shown the presence of a logarithmic correction to the area law. Using the inertia moment density  $I(L)$  and spin stiffness  $\rho_s(L)$  as inputs, we have found that the number of Goldstone modes, which is related to the coefficient of the logarithmic term, is four by fitting our modified scaling formula to the  $S_2(L)$ . These results indicate the existence of an emergent  $SO(5)$  symmetry at the transition point, which spontaneously breaks to  $O(4)$  in the thermodynamic limit but restored in a finite size. This result demonstrates that the believed DQCP of the  $J-Q_3$  model is a weak first-order transition point. We have also found that the transition point of the  $J-Q_2$  model has similar properties [49], suggesting the VBS-Néel transition in this model is also weakly first order.

With this work, we have provided a new way to distinguish an ordered phase with continuous symmetry broken from a critical phase, which is potentially useful to identify other weak first-order phase transitions, which are hard to determine using conventional methods.

This work was supported by the National Nat-

ural Science Foundation of China under Grant No. 12175015, No. 12304171, No. 12088101 and MOST 2022YFA1402701 and the Beijing Institute of Technology Research Fund Program for Young Scholars. The authors acknowledge the support of Tianhe 2JK at the Beijing Computational Science Research Center(CSRC) and the Super Computing Center of Beijing Normal University.

\* The two authors contributed equally to this work.

† [waguo@bnu.edu.cn](mailto:waguo@bnu.edu.cn)

‡ [hqlin@zju.edu.cn](mailto:hqlin@zju.edu.cn)

- [1] T. Senthil, A. Vishwanath, L. Balents, S. Sachdev, and M. P. A. Fisher, Deconfined quantum critical points, *Science* **303**, 1490 (2004), <https://www.science.org/doi/pdf/10.1126/science.1091806>.
- [2] T. Senthil, L. Balents, S. Sachdev, A. Vishwanath, and M. P. A. Fisher, Quantum criticality beyond the landau-ginzburg-wilson paradigm, *Phys. Rev. B* **70**, 144407 (2004).
- [3] A. W. Sandvik, Evidence for deconfined quantum criticality in a two-dimensional heisenberg model with four-spin interactions, *Phys. Rev. Lett.* **98**, 227202 (2007).
- [4] J. Lou, A. W. Sandvik, and N. Kawashima, Antiferromagnetic to valence-bond-solid transitions in two-dimensional  $SU(n)$  heisenberg models with multispin interactions, *Phys. Rev. B* **80**, 180414 (2009).
- [5] R. G. Melko and R. K. Kaul, Scaling in the fan of an unconventional quantum critical point, *Phys. Rev. Lett.* **100**, 017203 (2008).
- [6] R. K. Kaul, Quantum criticality in  $su(3)$  and  $su(4)$  antiferromagnets, *Phys. Rev. B* **84**, 054407 (2011).
- [7] K. Harada, T. Suzuki, T. Okubo, H. Matsuo, J. Lou, H. Watanabe, S. Todo, and N. Kawashima, Possibility of deconfined criticality in  $su(n)$  heisenberg models at small  $n$ , *Phys. Rev. B* **88**, 220408 (2013).
- [8] S. Pujari, F. Alet, and K. Damle, Transitions to valence-bond solid order in a honeycomb lattice antiferromagnet, *Phys. Rev. B* **91**, 104411 (2015).
- [9] H. Shao, W. Guo, and A. W. Sandvik, Quantum criticality with two length scales, *Science* **352**, 213 (2016), <https://www.science.org/doi/pdf/10.1126/science.aad5007>.
- [10] A. Nahum, J. T. Chalker, P. Serna, M. Ortuño, and A. M. Somoza, Deconfined quantum criticality, scaling violations, and classical loop models, *Phys. Rev. X* **5**, 041048 (2015).
- [11] Y. Liu, Z. Wang, T. Sato, M. Hohenadler, C. Wang, W. Guo, and F. F. Assaad, Superconductivity from the condensation of topological defects in a quantum spin-hall insulator, *Nature Communications* **10**, 2658 (2019).
- [12] Y.-R. Shu, S.-K. Jian, and S. Yin, Nonequilibrium dynamics of deconfined quantum critical point in imaginary time, *Phys. Rev. Lett.* **128**, 020601 (2022).
- [13] T. Senthil and M. P. A. Fisher, Competing orders, nonlinear sigma models, and topological terms in quantum magnets, *Phys. Rev. B* **74**, 064405 (2006).
- [14] A. Nahum, P. Serna, J. T. Chalker, M. Ortuño, and A. M. Somoza, Emergent  $so(5)$  symmetry at the néel to valence-bond-solid transition, *Phys. Rev. Lett.* **115**,

- 267203 (2015).
- [15] J. Takahashi and A. W. Sandvik, Valence-bond solids, vestigial order, and emergent  $so(5)$  symmetry in a two-dimensional quantum magnet, *Phys. Rev. Res.* **2**, 033459 (2020).
- [16] Y. Nakayama and T. Ohtsuki, Necessary condition for emergent symmetry from the conformal bootstrap, *Physical Review Letters* **117**, 131601 (2016).
- [17] A. W. Sandvik and B. Zhao, Consistent scaling exponents at the deconfined quantum-critical point\*, *Chinese Physics Letters* **37**, 057502 (2020).
- [18] A. Nahum, Note on wess-zumino-witten models and quasiuniversality in  $2 + 1$  dimensions, *Phys. Rev. B* **102**, 201116 (2020).
- [19] R. Ma and C. Wang, Theory of deconfined pseudocriticality, *Phys. Rev. B* **102**, 020407 (2020).
- [20] B. Zhao, J. Takahashi, and A. W. Sandvik, Multicritical deconfined quantum criticality and lifshitz point of a helical valence-bond phase, *Phys. Rev. Lett.* **125**, 257204 (2020).
- [21] D.-C. Lu, C. Xu, and Y.-Z. You, Self-duality protected multicriticality in deconfined quantum phase transitions, *Phys. Rev. B* **104**, 205142 (2021).
- [22] A. B. Kuklov, M. Matsumoto, N. V. Prokof'ev, B. V. Svistunov, and M. Troyer, Deconfined criticality: Generic first-order transition in the  $su(2)$  symmetry case, *Phys. Rev. Lett.* **101**, 050405 (2008).
- [23] K. Chen, Y. Huang, Y. Deng, A. B. Kuklov, N. V. Prokof'ev, and B. V. Svistunov, Deconfined criticality flow in the heisenberg model with ring-exchange interactions, *Phys. Rev. Lett.* **110**, 185701 (2013).
- [24] F.-J. Jiang, M. Nyfeler, S. Chandrasekharan, and U.-J. Wiese, From an antiferromagnet to a valence bond solid: evidence for a first-order phase transition, *Journal of Statistical Mechanics: Theory and Experiment* **2008**, P02009 (2008).
- [25] R. C. Myers and A. Sinha, Seeing a c-theorem with holography, *Phys. Rev. D* **82**, 046006 (2010).
- [26] J. Zhao, Y.-C. Wang, Z. Yan, M. Cheng, and Z. Y. Meng, Scaling of entanglement entropy at deconfined quantum criticality, *Phys. Rev. Lett.* **128**, 010601 (2022).
- [27] J. D'Emidio and A. W. Sandvik, Entanglement entropy and deconfined criticality: emergent  $so(5)$  symmetry with tilted bipartitions, (to be published).
- [28] H. Casini and M. Huerta, Universal terms for the entanglement entropy in  $2+1$  dimensions, *Nuclear Physics B* **764**, 183 (2007).
- [29] M. A. Metlitski and T. Grover, Entanglement Entropy of Systems with Spontaneously Broken Continuous Symmetry, arXiv e-prints, arXiv:1112.5166 (2011), arXiv:1112.5166 [cond-mat.str-el].
- [30] J. D'Emidio, Entanglement entropy from nonequilibrium work, *Phys. Rev. Lett.* **124**, 110602 (2020).
- [31] J. Zhao, B.-B. Chen, Y.-C. Wang, Z. Yan, M. Cheng, and Z. Y. Meng, Measuring rényi entanglement entropy with high efficiency and precision in quantum monte carlo simulations, *npj Quantum Materials* **7**, 69 (2022).
- [32] B. Kulchytskyy, C. M. Herdman, S. Inglis, and R. G. Melko, Detecting goldstone modes with entanglement entropy, *Phys. Rev. B* **92**, 115146 (2015).
- [33] Z. Deng, L. Liu, W. Guo, and H. Q. Lin, Improved scaling of the entanglement entropy of quantum antiferromagnetic heisenberg systems, *Phys. Rev. B* **108**, 125144 (2023).
- [34] M. Song, J. Zhao, Z. Y. Meng, C. Xu, and M. Cheng, Extracting subleading corrections in entanglement entropy at quantum phase transitions (2024), arXiv:2312.13498 [cond-mat.str-el].
- [35] B. Zhao, P. Weinberg, and A. W. Sandvik, Symmetry-enhanced discontinuous phase transition in a two-dimensional quantum magnet, *Nature Physics* **15**, 678 (2019).
- [36] Y.-C. Wang, N. Ma, M. Cheng, and Z. Y. Meng, Scaling of the disorder operator at deconfined quantum criticality, *SciPost Phys.* **13**, 123 (2022).
- [37] A. W. Sandvik, Ground state projection of quantum spin systems in the valence-bond basis, *Phys. Rev. Lett.* **95**, 207203 (2005).
- [38] A. W. Sandvik and H. G. Evertz, Loop updates for variational and projector quantum monte carlo simulations in the valence-bond basis, *Phys. Rev. B* **82**, 024407 (2010).
- [39] A. W. Sandvik, Finite-size scaling of the ground-state parameters of the two-dimensional heisenberg model, *Phys. Rev. B* **56**, 11678 (1997).
- [40] A. W. Sandvik, Computational studies of quantum spin systems, *AIP Conference Proceedings* **1297**, 135 (2010).
- [41] See Supplemental Material.
- [42] P. Hasenfratz and F. Niedermayer, Finite size and temperature effects in the af heisenberg model, *Zeitschrift für Physik B Condensed Matter* **92**, 91 (1993).
- [43] H. Neuberger and T. Ziman, Finite-size effects in heisenberg antiferromagnets, *Phys. Rev. B* **39**, 2608 (1989).
- [44] D. S. Fisher, Universality, low-temperature properties, and finite-size scaling in quantum antiferromagnets, *Phys. Rev. B* **39**, 11783 (1989).
- [45] C. Lavallo, S. Sorella, and A. Parola, Anomalous finite size spectrum in the  $S = 1/2$  two dimensional heisenberg model, *Phys. Rev. Lett.* **80**, 1746 (1998).
- [46] O. F. Syljuåsen and A. W. Sandvik, Quantum monte carlo with directed loops, *Phys. Rev. E* **66**, 046701 (2002).
- [47] G. Gallup, Angular momentum in n-dimensional spaces, *Journal of Molecular Spectroscopy* **3**, 673 (1959).
- [48] R. Eder, W. Hanke, and S.-C. Zhang, Numerical evidence for  $so(5)$  symmetry and superspin multiplets in the two-dimensional  $t-j$  model, *Phys. Rev. B* **57**, 13781 (1998).
- [49] Z. Deng, L. Liu, W. Guo, and H. Q. Lin, (to be published).

**SUPPLEMENTAL MATERIAL**

**Additional scaling analysis at  $Q/J = 1.49153$**

Here, we present additional fitting results of Eq. (2) to  $S_2(L)$  at  $Q/J = 1.49153$ . In the main text,  $I(L, S = 1)$  is used as known finite-size inertia moment density  $I(L)$ . Table IV and V present results of fitting to  $S_2(L)$  using  $I(L, S = 2)$  and  $I(L, S = 3)$  as  $I(L)$ , respectively. The fits remain stable upon further excluding small size points by increasing  $L_{min}$  gradually, although error bars on the fit parameters increase rapidly. We obtain  $N_G/2 = 2.03(14)$  and  $2.01(14)$ , in the best estimations. We find that our modified formula works for  $I(L, S = 2)$  and  $I(L, S = 3)$ , which give the same results as that of  $I(L, S = 1)$ .

TABLE IV. Fitting results of Eq. (2) to  $S_2(L)$  at  $Q/J = 1.49153$ . In the fits, finite-size  $\rho_s(L)$  and  $I(L, S = 2)$  are used as inputs. The range of the system sizes is from  $L = 8$  to  $L = 48$ .

$L_{min}$	$a$	$b$	$\gamma_{ord}$	$\chi_r^2/P$ -value
12	0.2533(3)	2.00(4)	1.15(2)	1.33/0.23
16	0.2539(4)	1.89(6)	1.09(3)	0.60/0.73
20	0.2538(5)	1.91(10)	1.10(5)	0.71/0.61
24	0.2532(7)	2.03(14)	1.16(7)	0.54/0.70
28	0.2526(11)	2.16(24)	1.22(12)	0.58/0.63

TABLE V. Fitting results of Eq. (2) to  $S_2(L)$  at  $Q/J = 1.49153$ . In the fits, finite-size  $\rho_s(L)$  and  $I(L, S = 3)$  are used as inputs. The range of the system sizes is from  $L = 8$  to  $L = 48$ .

$L_{min}$	$a$	$b$	$\gamma_{ord}$	$\chi_r^2/P$ -value
12	0.2531(3)	2.02(4)	1.15(2)	1.89/0.07
16	0.2538(3)	1.88(6)	1.07(3)	0.54/0.77
20	0.2538(5)	1.88(10)	1.07(5)	0.65/0.66
24	0.2532(7)	2.01(14)	1.13(12)	0.43/0.79
28	0.2527(11)	2.13(24)	1.20(12)	0.45/0.72

Here, we analyze the finite-size behavior of  $I(L, S)$  and  $\rho_s(L)$ . Table VI shows a polynomial fit to  $I(L, S = 1)$  (shown in Fig. 5). We find  $I(L, S = 1)$  converges to a small but finite value, ten times larger than the error bars. Table VII shows a polynomial fit to  $\rho_s(L)$  (shown in Fig. 3). We see  $\rho_s(L)$  converges to a finite value.

TABLE VI. Polynomial fit  $I(L) = a + b/L + c/L^2$  to the data of  $I(L, S = 1)$ .

$L_{min}$	$a$	$b$	$c$	$\chi_r^2/P$ -value
16	0.000461(8)	0.1681(4)	-0.191(5)	1.26/0.27
20	0.000448(13)	0.1690(8)	-0.203(10)	1.17/0.32
24	0.000417(22)	0.1711(14)	-0.237(21)	0.64/0.64
28	0.000417(40)	0.1711(29)	-0.237(50)	0.85/0.47

TABLE VII. Polynomial fit  $\rho_s(L) = a + b/L + c/L^2$  to the data of  $\rho_s(L)$ .

$L_{min}$	$a$	$b$	$c$	$\chi_r^2/P$ -value
20	0.0129(3)	2.54(2)	-5.0(2)	1.63/0.15
24	0.0124(5)	2.57(3)	-5.5(5)	1.68/0.15
28	0.0114(8)	2.64(6)	-6.9(10)	1.48/0.22

TABLE VIII. Power-law fit  $I(L) = aL^b$  to the data of  $I(L, S = 1)$ .

$L_{min}$	$a$	$b$	$\chi_r^2/P$ -value
24	0.1174(3)	-0.881(1)	1.26/0.27
28	0.1166(5)	-0.879(1)	1.60/0.17
32	0.1155(8)	-0.877(2)	1.07/0.36

However, power-law fitting to  $I(L, S)$  and  $\rho_s(L)$  are also possible for sufficiently large  $L_{min} = 24$  and  $28$ , respectively. For sufficient large  $L_{min}$ , the fits are also statistically sound. The results are listed in Tab. VIII and Tab. IX.

For conventional  $(2 + 1)$ D critical behavior,  $\rho_s(L)$  should scale as  $1/L$ . It has been found that  $L\rho_s$  diverges slowly at the VBS-Néel transition point of the  $J - Q_2$  model [24]. One interpretation of this unusual scaling behavior is that the transition is first order. The scaling is also explained by an unconventional two-length scales scaling scheme[9], with  $\rho_s(L) \sim L^{-\nu/\nu'} \sim L^{-0.715}$ , where  $\nu$  and  $\nu'$  are the correlation length exponent and the exponent associated with the divergence of the thickness of VBS domain wall, respectively. Here we find similar scaling behavior of  $\rho_s(L)$  for the  $J - Q_3$  model with an exponent close to that in the  $J - Q_2$  model. However, in this work, we do not try to determine or explain the finite-size scaling behavior of  $\rho_s(L)$  and  $I(L, S)$ . Instead, we use the finite-size value of  $\rho_s(L)$  and  $I(L, S)$  as inputs of the fitting formula Eq. (2). The results of the fits, in turn, support  $I(L)$  and  $\rho_s(L)$  have finite values at thermodynamic limit.

TABLE IX. Power-law fit  $\rho_s(L) = aL^b$  to the data of  $\rho_s(L)$ .

$L_{min}$	$a$	$b$	$\chi_r^2/P$ -value
28	1.339(8)	-0.788(2)	1.61/0.17
32	1.322(11)	-0.784(3)	0.84/0.47
36	1.330(18)	-0.786(4)	1.11/0.33

**Scaling analyses at  $Q/J = 1.489$**

Here we present results for  $S_2(L)$ ,  $\rho_s(L)$ , and  $I(L, S)$  at  $Q/J = 1.489$ .

Figure 7 shows  $S_2(L)/L$  versus system size  $L$  at  $Q/J = 1.489$ . Table X shows fits to  $S_2(L)$  without logarithmic corrections. Fits using Eq. (11) to the same set of data

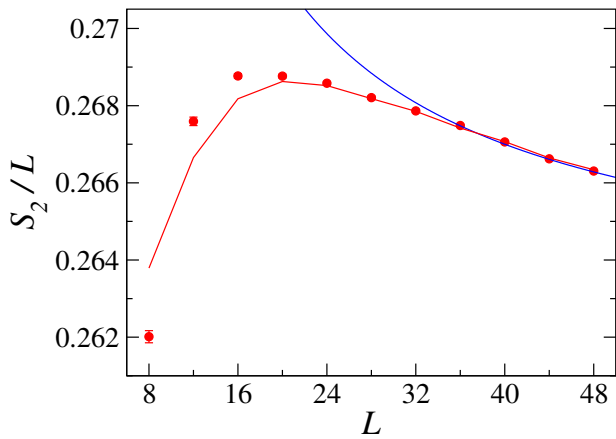


FIG. 7.  $S_2(L)/L$  vs  $L$  at  $Q/J = 1.489$ . The red solid line is the fit using Eq. 2 for  $L \geq L_{min} = 20$ , see Tab. XIII. The blue solid line shows a fit without logarithmic correction for  $L \geq L_{min} = 36$

$S_2(L)$  are listed in Tab. XI. The presence of the logarithmic term is apparent.

TABLE X. Fits without logarithmic correction  $S(L) = aL + c$  to the  $S_2(L)$  data at  $Q/J = 1.489$ .

$L_{min}$	$a$	$c$	$\chi_r^2/\text{P-value}$
36	0.2627(2)	0.172(6)	0.84/0.43
40	0.2625(3)	0.182(11)	0.40/0.52

TABLE XI. Fits using Eq. (11) to the  $S_2(L)$  data.

$L_{min}$	$a$	$b$	$c$	$\chi_r^2/\text{P-value}$
8	0.2584(1)	0.197(3)	-0.380(6)	2.04/0.037
12	0.2584(2)	0.195(5)	-0.377(11)	2.32/0.023
16	0.2582(3)	0.203(7)	-0.394(16)	2.37/0.028
20	0.2573(4)	0.231(12)	-0.464(28)	1.05/0.39
24	0.2568(6)	0.248(20)	-0.508(50)	1.02/0.40

Table XII, XIII, and XIV show fitting results of Eq. (2) to the  $S_2(L)$ , using  $I(L, S = 1)$ ,  $I(L, S = 2)$ , and  $I(L, S = 3)$  as inputs, respectively. These fits all give  $N_G/2 = 2$  within an error bar of 10%, suggesting the  $SO(5)$  symmetry breaking at a first-order transition.

We now present finite-size behavior analysis of  $I(L, S)$  and  $\rho_s(L)$  here.

The total magnetization as a function of the external field at  $Q/J = 1.489$  for various system sizes is shown in Fig. 8. We can estimate  $I(L, S)$ , with  $S = 1, 2, 3$  from these data. The results are shown in Fig. 9.

Table XV shows a polynomial fit to  $I(L, S = 1)$ , as shown in Fig. 9. Again, we see  $I(L, S = 1)$  converges to a small but finite value, much larger than the error bars.

The calculated spin stiffness  $\rho_s(L)$  at  $Q/J = 1.489$  are shown in Fig. 10.

TABLE XII. Fits using Eq. (2) to the  $S_2(L)$  data, in which  $I(L, S = 1)$  are used as inputs.

$L_{min}$	$a$	$b$	$\gamma_{ord}$	$\chi_r^2/\text{P-value}$
12	0.2549(3)	1.74(4)	1.01(2)	2.00/0.05
16	0.2551(4)	1.71(6)	1.00(3)	2.23/0.04
20	0.2539(6)	1.96(10)	1.12(5)	0.80/0.55
24	0.2532(9)	2.07(17)	1.18(9)	0.81/0.52
28	0.2525(14)	2.22(28)	1.25(14)	0.95/0.42

TABLE XIII. Fits using Eq. (2) to the  $S_2(L)$  data, in which  $I(L, S = 2)$  are used as inputs.

$L_{min}$	$a$	$b$	$\gamma_{ord}$	$\chi_r^2/\text{P-value}$
12	0.2545(3)	1.83(5)	1.05(3)	2.27/0.03
16	0.2549(4)	1.75(6)	1.01(3)	1.99/0.06
20	0.2537(6)	1.97(10)	1.12(5)	0.82/0.54
24	0.2531(9)	2.09(17)	1.18(9)	0.85/0.50
28	0.2527(14)	2.19(28)	1.23(14)	1.06/0.36

Table XVII shows a polynomial fit to  $\rho_s(L)$ . We see  $\rho_s(L)$  converges to a finite value.

Similar to  $Q/J = 1.49153$ , power-law fitting to  $I(L, S = 1)$  and  $\rho_s(L)$  is also possible for sufficient large  $L_{min}$ , although these  $L_{min}$  are much larger than those used for polynomial fitting. The fit results are listed in Tab. XVI and XVIII, respectively. The slow diverging of  $L\rho_s$  is seen. Again, this behavior is at odds with the conventional  $(2 + 1)\text{D}$  critical behavior:  $\rho_s(L) \propto 1/L$ . Different interpretations are present. Still, We do not try to determine or explain the finite-size scaling behavior of  $\rho_s(L)$ . Instead, we use the finite-size value of  $\rho_s(L)$  and  $I(L, S)$  as inputs of the fitting formula Eq. (2). The results of the fits, in turn, support  $I(L)$  and  $\rho_s(L)$  have finite values at the thermodynamic limit.

TABLE XIV. Fits using Eq. (2) to the  $S_2(L)$  data, in which  $I(L, S = 3)$  are used as inputs.

$L_{min}$	$a$	$b$	$\gamma_{ord}$	$\chi_r^2/\text{P-value}$
12	0.2544(3)	1.83(5)	1.04(3)	2.58/0.01
16	0.2550(4)	1.72(6)	0.99(3)	1.76/0.1
20	0.2539(6)	1.93(10)	1.09(5)	0.77/0.57
24	0.2533(9)	2.03(16)	1.14(8)	0.80/0.53
28	0.2529(14)	2.12(27)	1.18(14)	1.01/0.39

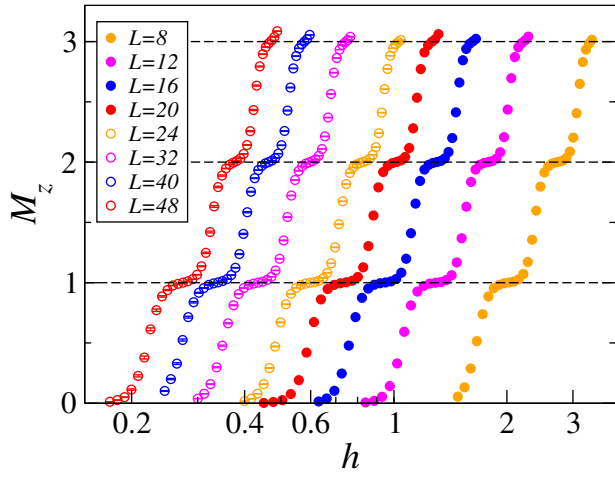


FIG. 8. Total magnetization  $M_z$  vs external field  $h$  at  $Q/J = 1.489$  for different system size  $L$ .

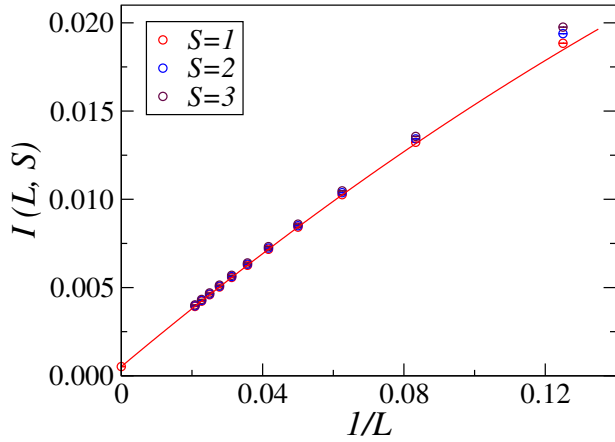


FIG. 9.  $I(L, S)$  versus  $L$  at  $Q/J = 1.489$ .  $I(L, S)$  for different  $S$  converges to the same value at large  $L$ , showing the emergence of  $SO(5)$  symmetry. The red solid line shows a polynomial fit to data points with  $L \geq 20$  with  $I(L = \infty, S = 1)$  found to be  $0.00052(1)$ , see Tab. XV.

TABLE XV. Polynomial fit  $I(L) = a + b/L + c/L^2$  to the data of  $I(L, S = 1)$ .

$L_{min}$	$a$	$b$	$c$	$\chi_r^2/P$ -value
16	0.000542(6)	0.1663(3)	-0.173(4)	1.84/0.09
20	0.000521(10)	0.1677(6)	-0.193(8)	0.82/0.54
24	0.000505(15)	0.1688(10)	-0.212(15)	0.46/0.77
28	0.000516(26)	0.1680(18)	-0.197(32)	0.51/0.67

TABLE XVI. Power-law fit  $I(L) = aL^b$  to the data of  $I(L, S = 1)$ .

$L_{min}$	$a$	$b$	$\chi_r^2/P$ -value
36	0.1093(7)	-0.859(2)	3.10/0.045
40	0.1071(14)	-0.854(3)	2.96/0.09

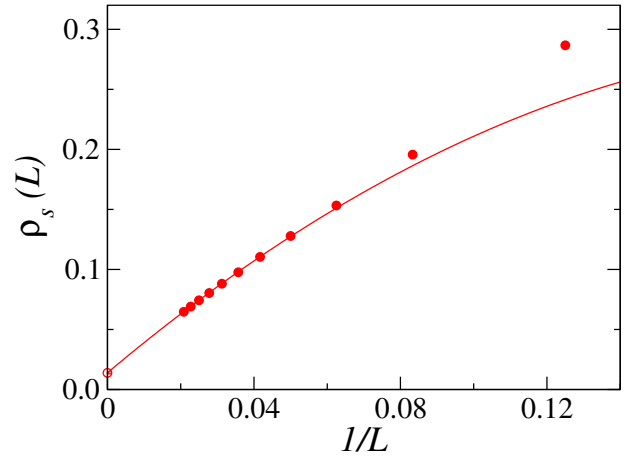


FIG. 10. Spin stiffness  $\rho_s(L)$  versus  $1/L$  at  $Q/J = 1.489$ . The red line is a polynomial fit for data points with  $L \geq 28$ .

TABLE XVII. Polynomial fit  $\rho_s(L) = a + b/L + c/L^2$  to the data of  $\rho_s(L)$ .

$L_{min}$	$a$	$b$	$c$	$\chi_r^2/P$ -value
24	0.0153(5)	2.46(3)	-4.4(5)	2.47/0.04
28	0.0139(8)	2.57(6)	-6(1)	1.60/0.19
32	0.0151(14)	2.48(11)	-4(2)	1.91/0.15

TABLE XVIII. Power-law fit  $\rho_s(L) = aL^b$  to the data of  $\rho_s(L)$ .

$L_{min}$	$a$	$b$	$\chi_r^2/P$ -value
36	1.20(2)	-0.754(4)	1.54/0.22
40	1.20(3)	-0.755(6)	3.04/0.08